Journal of Materials Research and Technology 30 (2024) 640–656

Contents lists available at ScienceDirect

Journal of Materials Research and Technology

journal homepage: www.elsevier.com/locate/jmrt

Novel high nitrogen austenitic stainless steels: From high-throughput screening to experimental validation and properties relationship

Victor Hugo Mafra Monfredo Ferreira [a,b,*], Francisco Gil Coury [a,b], Diego de Araujo Santana [a,b], Guilherme Yuuki Koga [a,b,c]

[a] Federal University of São Carlos, Graduate Program in Materials Science and Engineering, Rod. Washington Luis, Km 235, CEP 13565-905, São Carlos, SP, Brazil
[b] Federal University of São Carlos, Department of Materials Science and Engineering, Rod. Washington Luis, São Carlos, SP, CEP 13565–905, Brazil
[c] Federal University of São Carlos, Center for Characterization and Development of Materials (CCDM), Rod. Washington Luis, São Carlos, SP, CEP 13565–905, Brazil
Washington Luis, São Carlos, SP, CEP 13565–905, Brazil

ARTICLE INFO

Keywords:
Alloy design
CALPHAD
Manganese
Nitrogen
Mechanical properties
Corrosion

ABSTRACT

The quest for affordable and price-stable alternatives for nickel as the main austenitizing alloying element is pushing the stainless steel industries to develop new types of Ni-lean austenitic stainless steels. This work focuses on the challenges of designing austenitic stainless steels with appreciable nitrogen content using computational methods, which can still be produced at 1 atm N_2 pressure and thermomechanically processed without excessive cracking or N_2 degassing. CALPHAD-based computational tools enabled the identification of promising alloys by high-throughput screening from more than 2000 candidates based on predefined criteria considering composition (Ni-poor, N-rich), phase stability (austenite), degassing (far from N_2 loss from liquid or solid phase), cost (Ni-lean), and pitting resistance equivalent number (PREN > AISI 201 stainless steel). The resulting alloys exhibited an austenitic microstructure with dispersed micrometric and nanometric aluminum nitrides (AlN) precipitates. Even with the occurrence of appreciable AIN precipitates, hot rolling was performed without cracking, resulting in equiaxed austenitic grains. The mechanical properties of the developed alloys exceeded those of AISI 201 stainless steel in terms of hardness, yield strength, and ultimate tensile strength, with values of 304 HV, 534 MPa, and 953 MPa, respectively, yet with considerable ductility (~40% elongation). Even in the presence of AlN that pick up some of the nitrogen from solid solution, the corrosion resistance of the developed alloy was superior to the AISI 201 stainless steel. This research provides valuable insights for developing and processing high-nitrogen austenitic stainless steels to compete with 201 and 304 stainless steels in terms of mechanical properties and corrosion resistance.

1. Introduction

Nitrogen is an austenitizing alloying element in stainless steels that can partially replace nickel. Nitrogen is an effective solid solution hardening agent, increasing both yield strength and ultimate tensile strength in these steels and improving wear and fatigue resistance [1]. Furthermore, the addition of nitrogen can result in grain size refinement, strong austenite stabilization (reducing the tendency to form stress-induced martensite), and improvement of the corrosion resistance of the steel. Additionally, nitrogen has a significant effect on the repassivation process after the original passivation film is damaged [2] and also improves the effects that other alloying elements, such as chromium and molybdenum, have on corrosion resistance [3].

Despite all the benefits, other austenitizing alloying elements dominate, such as nickel for the 3XX and manganese for 2XX type stainless steels because of the challenges of the processing of high-nitrogen stainless steels. Two main challenges are imposed to take advantage of the beneficial properties of nitrogen: (1) how to obtain high nitrogen content in the melt, and (2) how to keep it in solution during solidification and solid-state transformations. The solubility of nitrogen in stainless steels depends, for practical steel making purposes, on three main parameters: temperature, alloy composition, and pressure [4,5]. Therefore, the application of predictive methods is essential to foresee the type of predominant phase in steels.

* Corresponding author. Federal University of São Carlos, Graduate Program in Materials Science and Engineering, Rod. Washington Luis, km 235, CEP 13565-905, São Carlos, SP, Brazil.
E-mail address: victormonfredo@estudante.ufscar.br (V.H. Mafra Monfredo Ferreira).

https://doi.org/10.1016/j.jmrt.2024.03.090
Received 25 January 2024; Received in revised form 12 March 2024; Accepted 14 March 2024
Available online 15 March 2024

The equivalent method considers the constitution diagram covering austenite, ferrite, and martensite, as their overlapping phase fields. Through weighted sums of elements that stabilize austenite and ferrite, combined with empirical coefficients derived from experimental data, the equivalent contents of Ni and Cr are determined, allowing for an estimation of the structure's stability [6].

The Schaeffler diagram is a useful tool for predicting the microstructure of alloys, but it has also some limitations. One of the main drawbacks of the Schaeffler diagram is being based on linear interpolation between binary systems, which can lead to inaccuracies when predicting the phases present in multicomponent alloys. Additionally, the Schaeffler diagram is limited to predicting the microstructure of alloys in the solid state, and it is not accurate to predict the stable phases in other states and mixtures, such as liquids or gaseous alloys.

The trial-and-error method for alloy design relies solely on empirical data, without considering the underlying physical and chemical processes that influence the behavior of an alloy. Additionally, the trial-and-error method is time-consuming and can be expensive, as it involves the synthesis of multiple alloys and the characterization of their properties through extensive testing.

The CALPHAD (Calculation of Phase Diagrams) method is well established for alloy design. It is a computational approach that uses thermodynamic and kinetic models to predict the phase equilibria and thermodynamic properties of alloys [7]. It allows a detailed understanding of the thermodynamic properties of a wide range of alloys, including those in the solid, liquid, and gaseous states. Additionally, the CALPHAD method enables the evaluation of phase stability under different thermodynamic variables, such as temperature and pressure.

High Nitrogen Stainless Steels (HNSS) often exhibits a narrow single phase temperature range, which is important for its thermomechanical processing. Furthermore, it is often susceptible to a high possibility of deleterious phases formation, further complicating its processing. For example, the hot working temperature range for an 18Cr–18Mn-0.6 N alloy is between 1050 and 1100 °C, with intergranular cracking occurring below this temperature given the excessive precipitation of Cr_2N at the grain boundaries of austenite [8]. Therefore, understanding the ranges of phase formation and decomposition is crucial for the thermomechanical processing of HNSSs, as well as knowing whether the nitrogen content is in solid solution, given that elements that increase nitrogen solubility, such as Ti, Zr, V, Nb, and Cr, tend to form nitrides that can embrittle the alloy.

This work aims to uncover the challenges of developing and thermomechanically processing high-nitrogen stainless steels in the context of reducing the nickel content as main austenitizing element of 3XX stainless steels. For this purpose, high-throughput CALPHAD thermodynamic calculations were used to explore a vast field of novel high-nitrogen stainless steels to identify promising alloys based on elements that: i) ensure austenitic microstructure, ii) positively influence the solubility of nitrogen, iii) reduce the demand of Ni, and iv) maintain an elevated Pitting Resistance Equivalent Number (PREN) index. The alloy was vacuum induced melted, homogenized, hot rolled, cold rolled and recrystallized i.e., followed key step of thermomechanical manufacturing processes of stainless steel plates. The microstructural features were characterized by multiple methods, and correlated to the mechanical and corrosion properties, compared to commercial AISI 304 and 201 stainless steels. The results pointed out to the opportunities and challenges of using high nitrogen content to design novel austenitic stainless steels, and how to avoid potential pitfalls normally seen during experimentation, aiming guiding more consistent and reliable manufacturing processes.

2. Experimental

2.1. High-throughput calculation

Computational thermodynamic calculations were performed using the CALPHAD method assisted by two different softwares, Pandat™ and Thermo-calc™. The database used in the Pandat™ software was the PanFe2022a, as it covers 96% of the binary system considering the main elements of the steel of interest (Fe, Cr, Mn, Ni, N, C, Si, Cu), while the Thermo-calc™ database used was the TCFE9, which covers all binaries across the entire composition and temperature range of interest.

The alloys of interest were designed to balance the mechanical properties of AISI 201 SS with the corrosion resistance of AISI 304 SS. Manganese and nitrogen were used for reducing the nickel content, while still maintaining the austenitic structure, and improving the mechanical properties. Alloy compositions were selected through the incorporation of predefined criteria based on literature and commercial alloys. Fig. 1 summarizes the thermodynamic calculations steps.

First, the compositional space for alloying was selected based on the commercial 201 and 304 stainless steels according to Ref. [9], along with extrapolations of their compositions as detailed in (Table 1).

The initial calculations, considering only the elemental content, resulted in 2304 alloys. Then, the following filtering criteria were applied based on the calculated phase diagrams: no sigma (σ) phase above 750 °C, having a large single-phase face-centered cubic (FCC), not having carbides (M_7C_3 and $M_{23}C_6$) above 960 °C, and α-ferrite above 600 °C. These criteria were defined based on the equilibrium phase diagrams of the 304 and 201 stainless steels. After filtering, the number of compositions was reduced to 366 alloys.

In the pursuit of further data refinement, criteria such as the highest values of PREN and a nitrogen content range between 0.2 and 0.5% were employed. The PREN index considers the beneficial effects of Cr, Mo, and N on pitting corrosion resistance. However, the original empirical formula [10] does not account for the detrimental effect of Mn. Consequently, for single-phase austenitic stainless steels with high Mn content and low Ni content, the modified $PREN_{Mod}$ [11] (Cr + 3.3Mo + 16 N–0.5Mn) was used, resulting in the reduction of compositions to 217.

As the final criterion, the production cost of the alloy, based on costs of alloying elements sourced from commodity markets [12], was considered, resulting in the selection of 10 final compositions with the lowest cost values. Among these 10 final compositions, one was chosen based on higher $PREN_{Mod}$, N content, and lower cost considerations.

2.2. Alloy production

A 3 kg ingot of the selected alloy (20%Cr–14%Mn–5%Ni-0.5%N–2% Cu-0.01%C-0.5%Si–Fe) was produced by induction melting furnace, manufactured by Inductotherm, model VIP 50-30R Power Track, under a high-purity nitrogen atmosphere, to serve as a source of N supply in the liquid metal, and cast into a graphite crucible coated with alumina. The raw materials were an AISI 1004 steel and commercially pure Cr, Mn, Ni, Cu, and MnN. The latter was used as a source of nitrogen.

The as-cast alloy was homogenized for 8 h at 1250 °C. Next, the sample was hot rolled at approximately 1250 °C in multiple stages until the initial slab thickness of 10 mm was reduced to approximately 2–3 mm. After each rolling step, the sample was reheated to 1250 °C. In the final rolling, the sample was water quenched. Subsequently, cold rolling was performed to achieve a reduction of ~50%, followed by recrystallization at 1150 °C for 1 h and water quenching to ensure an austenitic structure neither with excessive grain growth nor the formation of chromium nitride. Fig. 2 shows a schematic flowchart for the alloy processing.

The nominal composition of the selected alloy is detailed in Table 2, together with the measured composition of the 304 SS and 201 SS used as comparison.

2.3. Structural characterization

High-energy synchrotron X-ray diffraction experiments (SXRD) were conducted at the P07 beamline of PETRA III, located at the Deutsches Elektronen-Synchrotron (DESY) in Hamburg, Germany. A fixed energy

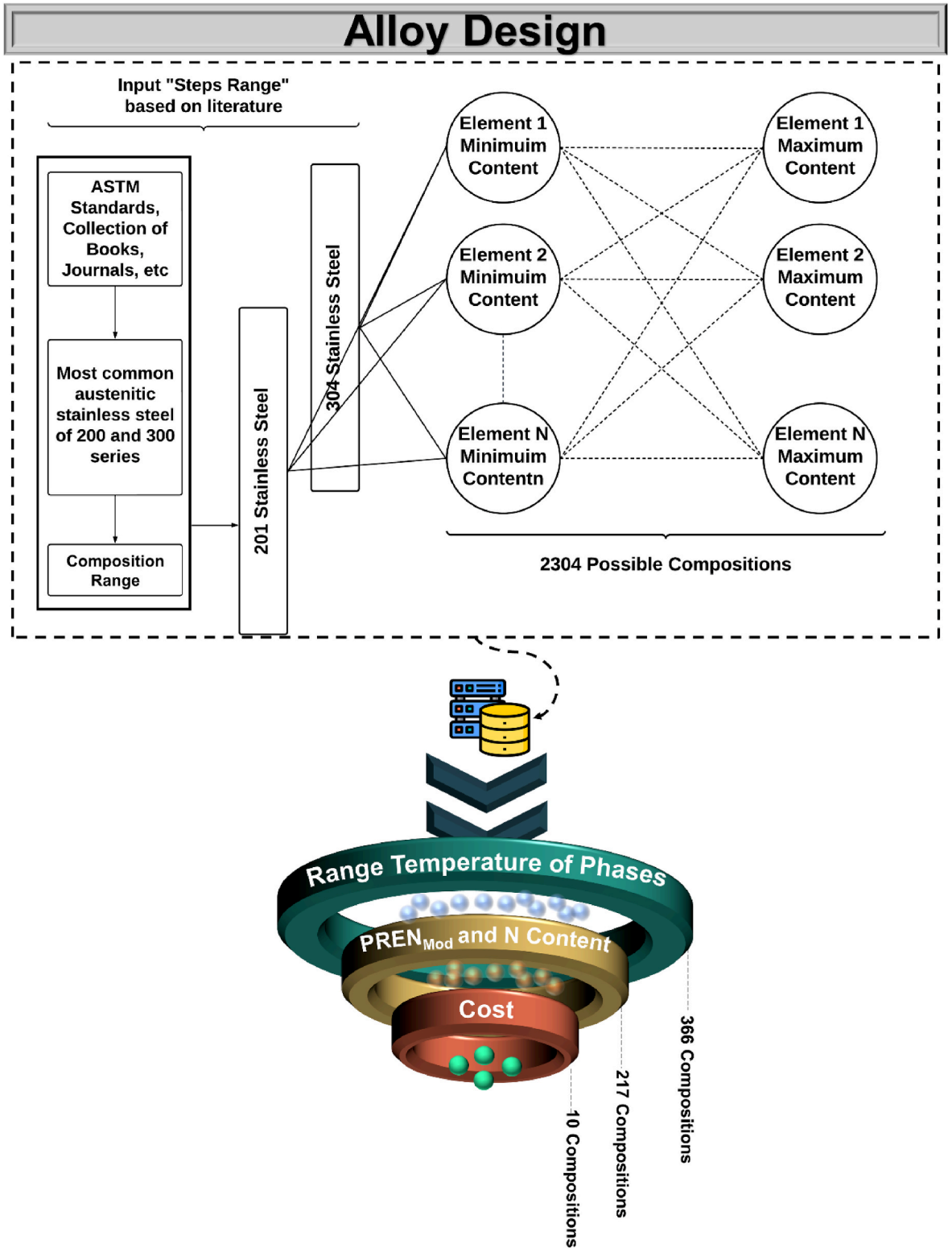

Fig. 1. Schematic for the HTC method used in this study, showing the creation of the compositional space from commercial databases using literature-based parameters, defining the total number of possible compositions along with the filters used for the selection of the most promising compositions.

of 87 keV, providing an X-ray wavelength of 0.142347 Å, was employed for structural characterization of the HNSS, including *ex-situ* and *in-situ* analysis with tensile tests. A small intensity 2nd harmonic of 174.2 keV, also can pass through the crystal monochromator, the reflections from this 2nd harmonic were considered in the data analysis.

The steel microstructure was characterized by optical microscopy (OLYMPUS BX41M-LED) and scanning electron microscopy (FEG-SEM, Philips, model XL30) using 25 kV acceleration voltage. Sample preparation for microstructural characterization was carried out by grinding the samples using Si–C sandpaper (from 220 to 1200 grit), polishing with 1 μm alumina suspension, and finally electrolytic etching with 10% oxalic (8 V for approximately 30s), following the standard

Table 1
Parameters used for the development of the compositional space in this study.

Elements (wt%)	Elemental content	Nº Steps
Mn (8–14%)	8/10/12/14	4x
C (0.01%)	1	1x
Si (0.5%)	1	1x
Ni (0–6%)	0/2/4/6	4x
N (0–0.52%)	0/0.07/0.13/0.2/0.26/0.33/0.39/0.45/0.52	9x
Cr (16–22%)	16/18/20/22	4x
Cu (0–3%)	0/1/2/3	4x
Total of Alloys' Candidates		**2304**

recommendations [13].

Electron backscattered diffraction (EBSD) technique was employed to analyze the microstructure and phases present in the alloy. The sample was grinded using Si–C paper to a grit size of 1200, and then polished with 1.0 μm alumina suspension. Additional sample polishing was carried out for 8 h in a colloidal silica solution using a Buehler Vibromet 2 polisher. The sample was analyzed using a FEG scanning electron microscope, Tescan Mira3, coupled with EBSD system. For chemical composition, energy-dispersive X-ray spectroscopy (EDS) analysis was performed.

The morphologies of the fine precipitates were characterized by transmission electron microscopy using a FEI Tecnai G^2 F20. Specimens for TEM were cut and grinded to a thickness of 50 μm. Thin foils were prepared in a precision ionic polishing system (PIPS) in a Gatan model 691. The sample was examined using TEM operating at 200 kV in diffraction contrast. For chemical compositions, STEM-EDS analysis was performed.

The steel compositions were determined using Spark Optical Emission Spectrometry (S-OES) on a SPECTROMAXx instrument, except the N, C, and S, which were measured by inert gas melting technique, and quantification by infrared in an induction furnace with thermoconductivity detection in a LECO ONH-836 and CS-844 equipment, respectively.

2.4. Mechanical properties

The uniaxial tensile tests were conducted at room temperature using an INSTRON 5900R testing machine, with strength rate of 8.11×10^{-4} s^{-1}. Three specimens of each alloy were machined to the dimensions shown in Fig. 3. The yield strength, ultimate tensile strength, and fracture strain were determined using pre-existing calculation subroutines in the INSTRON Bluehill software.

Due to the high energy of the photons and the intense flux of the P07

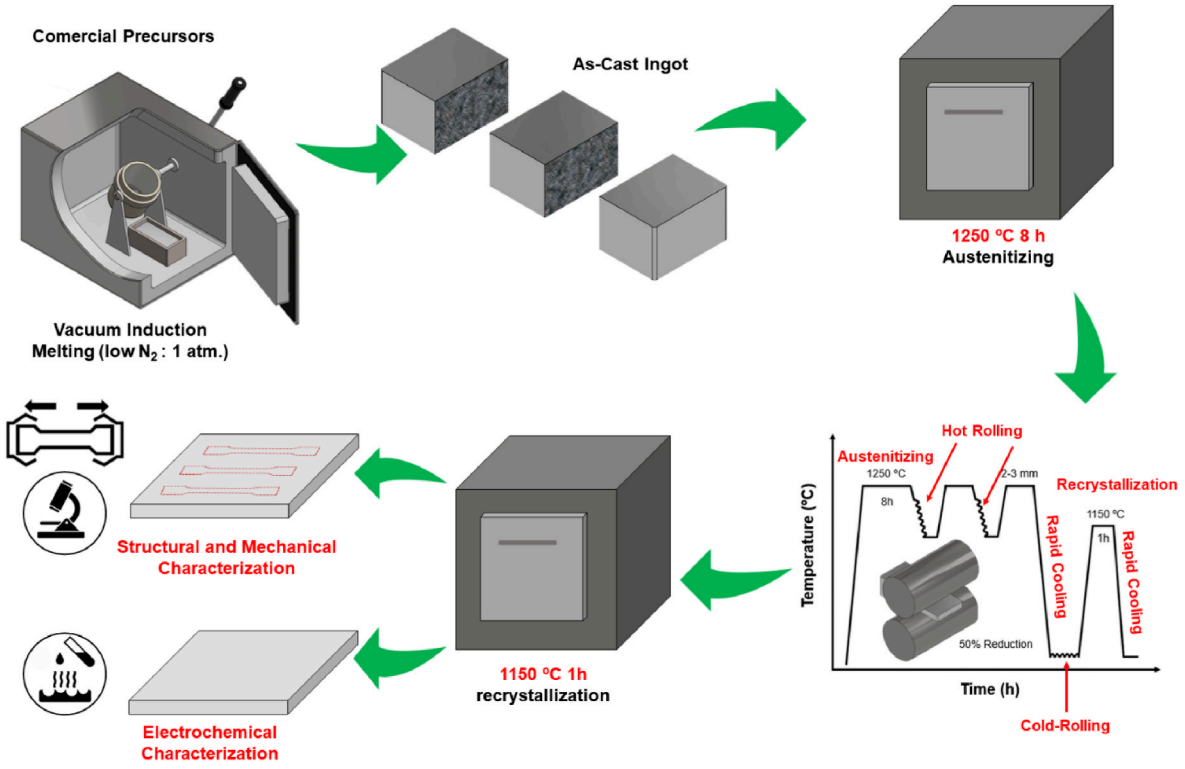

Fig. 2. Schematic diagram of the alloys processing steps.

Table 2
Nominal composition of the most promising high-nitrogen stainless steel (HNSS) obtained by HTC method. Measured composition of 304 SS and 201 SS used as comparison.

Composition (wt%)										
Sample	Fe	Cr	Mn	Ni	N	Cu	C	Si	Al	S
HNSS Nominal	Bal.	20	14	5	0.5	2	0.01	0.5	–	–
AISI 201 SS[a]	Bal.	17.5	6	4.22	0.16	0.05	0.03	1	0.01	0.0003
AISI 304 SS[a]	Bal.	18.3	1.2	8.2	0.05	0.15	0.02	0.04	0.005	0.002

[a] Elemental composition determined by park Optical Emission Spectrometry (S-OES). Interstitial elements (N, C, and S) measured by inert gas melting technique, and quantification by infrared in an induction furnace with thermoconductivity.

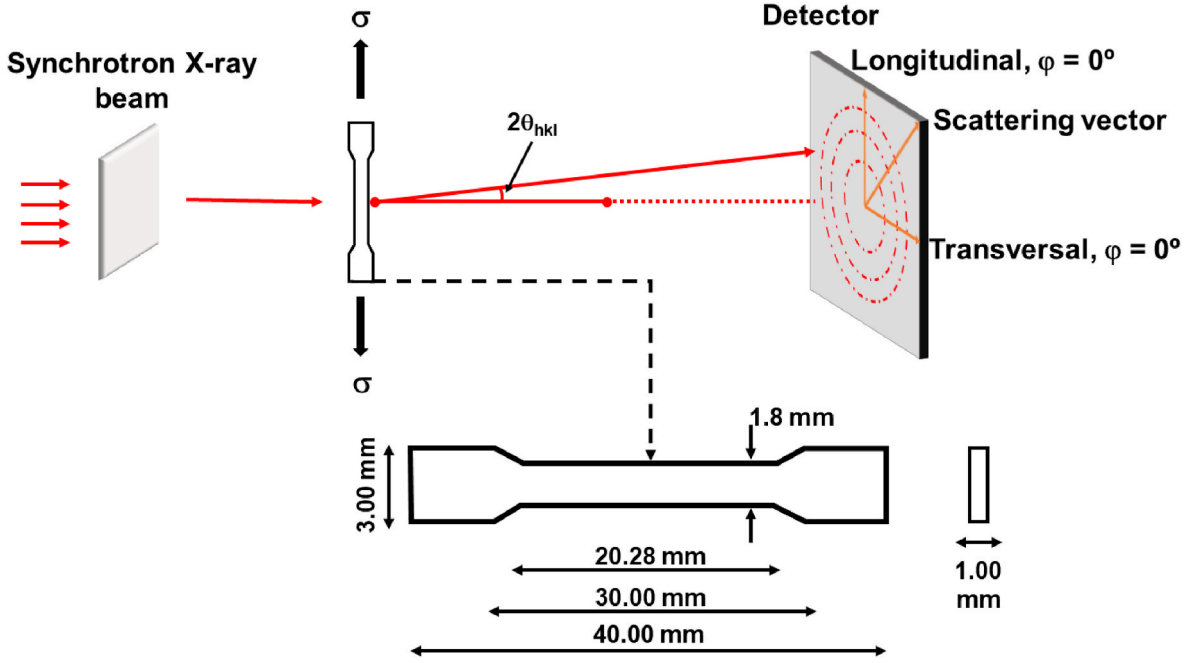

Fig. 3. Schematic illustration of the in situ tensile testing setup by Synchrotron X-ray, where $2\theta_{hkl}$ is the angle between the incident and diffracted beams.

beamline, it was possible to perform *in-situ* strain characterization, enabling the assessment of the structural transformation during loading. The material's behavior during deformation was thus investigated, allowing a clearer observation of the occurrence or absence of the Transformation-Induced Plasticity (TRIP) effect.

2.5. Corrosion measurements

The degree of sensitization of the HNSS, AISI 201 SS, and 304 SS were assessed from the double-loop electro-chemical potentiokinetic reactivation (DL-EPR) method, based on the International Standard [14], *Corrosion of metals and alloys – Electrochemical potentiokinetic reactivation measurement using the double loop method (based on the Cihal's method),* that guided the measurements of DL-EPR and DOS assessment. The electrolyte employed for the DL-EPR method was composed of 0.5 M H_2SO_4 + 0.01 M potassium thiocyanate (KSCN), prepared using demineralized water and high-purity reagents (H_2SO_4 95–98% P.A.; KSCN >95%). The working electrode was immersed in the solution for 15 min at the open circuit potential before commencing the anodic polarization, with a scan rate of 6 V/h, extending up to +300 mV_{SCE}. Subsequently, the scan was reversed back to the open circuit potential, employing a reverse scan rate of 6 V/h. The results from DL-EPR were presented in the form of linear *vs* linear plots, displaying the potential *vs.* current plot. The maximum current value attained during the forward anodic scan, known as the activation current (I_a), and the maximum value reached during the reverse scan towards the open circuit potential, referred to as the reactivation current (I_r), were documented. The percentage ratio of I_r to Ia (I_r/I_a, %) served as index of the degree of sensitization, according to the ISO 12732, 2006 guidelines: I_r/Ia <1% (unsensitized), I_r/I_a > 5% (sensitized), and 1% < I_r/I_a < 5% (slightly sensitized).

For a more definitive assessment, a supplementary test was conducted to evaluate the risk of intergranular corrosion based on [15] *Standard Practices for Detecting Susceptibility to Intergranular Attack in Austenitic Stainless Steels, Practice A*. The test involves an electrolytic attack in a 10% oxalic acid solution with a current density of 1 A cm^{-2} for 90 s on the polished sample's surface.

Electrochemical measurements in triplicate were performed using a three-electrode configuration, consisting of a saturated calomel electrode reference (SCE) and a platinum mesh as counter electrode (CE), along with a Gamry 600+ potentiostat. The working electrodes were alloys sanded on abrasive papers with grain sizes ranging from 220 to 1200 mesh, with an exposed area of 0.3 cm^2. A 3.5 wt% NaCl solution, consisting of high-purity NaCl (>99%) and deionized water, was employed as the standard chloride-rich electrolyte. The experiments were conducted at room temperature in an open-air environment, with each condition analyzed three times to ensure repeatability. The polarization started after 1 h at open circuit potential (OCP), from which the anodic polarization was performed at 1 mV/s from −250 mV *vs* OCP until reaching a current density of 1 mA cm^{-2}, from which the scan was reversed to OCP at a rate of 1 mV/s back to OCP.

Electrochemical Impedance Spectrometry (EIS) was used as a complement, starting after 1 h at OCP, with the amplitude perturbation of ±10 mV, frequency range from 10^5 Hz to 10^{-2} Hz, 10 points per decade, being the testing performed thrice to ensure repeatability. Two approaches were used to analyze the experimental EIS data: i) the electric equivalent circuit (EEC) using the Gamry Echem Analyst, and ii) the Measurement Model (Version 3) software from Watson and Orazem [16], based on the linear regression approach, enabling the estimation of the polarization resistance and the capacitive-like responses from the system.

3. Results and discussion

3.1. Thermodynamic calculations

Fig. 4a reveals three regions of risk of nitrogen loss. The first is in the high temperatures of the melt (Liq + GAS field), where the nitrogen loss occurs from the excessive overheated molten alloy, being the strict control of heat input during casting required. The second risk is of the solid-state degassing (FCC + GAS field), normally avoided given the nitrogen content below the "nose" of the maximum solubility of this element in austenite. The third risk is a nitrogen depletion due to the formation of Cr_2N (see FCC + Cr_2N field), which can be avoided by rapid cooling from single phase FCC domain.

Furthermore, the nominal composition obtained through the HTC method underwent changes, as high-purity elements were considered in thermodynamic calculations. Small levels of impurity elements, such as

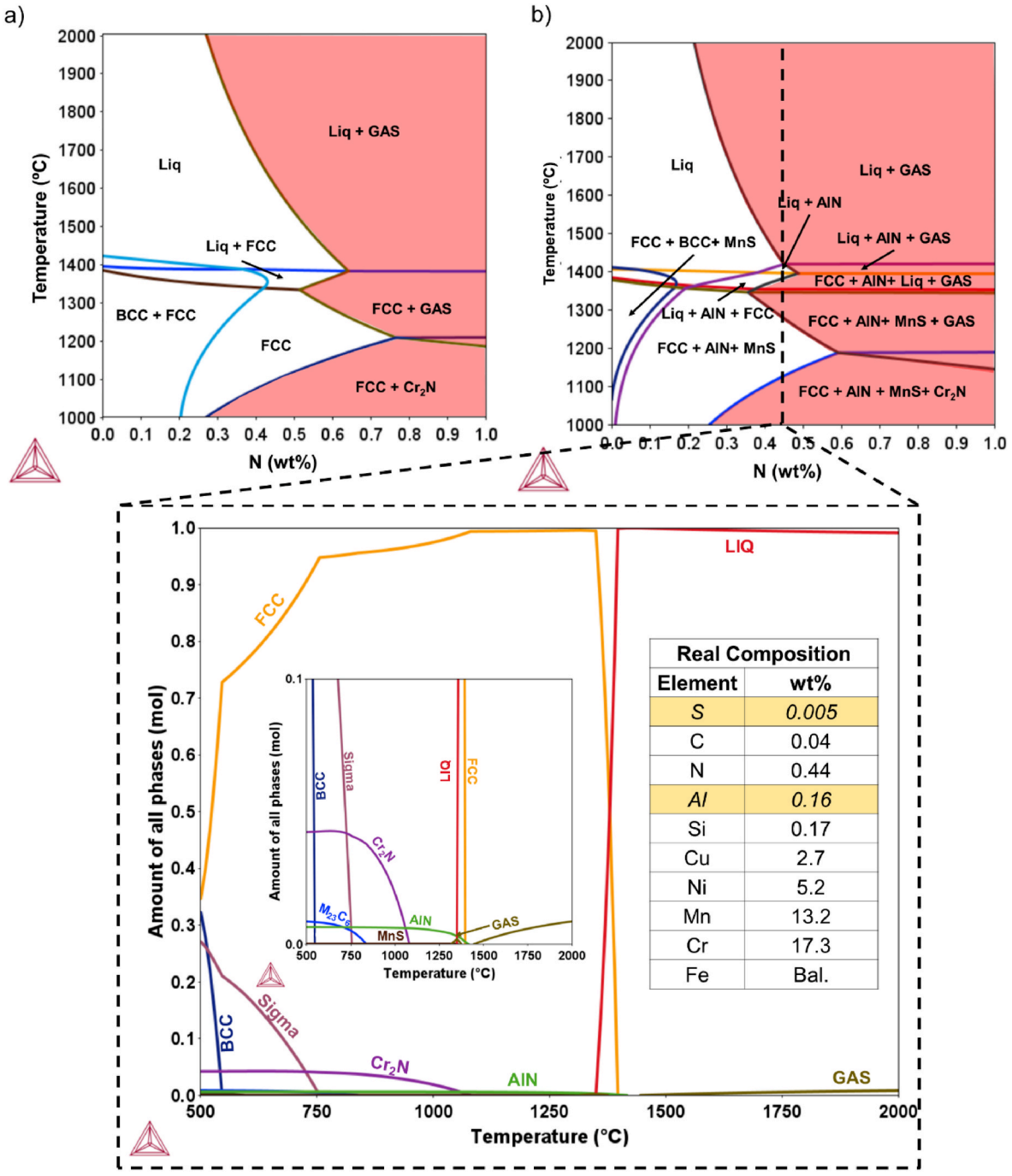

Fig. 4. Equilibrium diagram for HNSS alloy used in this study obtained through the CALPHAD method (Thermo-Calc software) with two different compositions: a) the nominal composition of the alloy, and b) The actual composition obtained through chemical analysis after the alloy's fabrication as detailed in the inserted Table.

aluminum (Al) and sulfur (S), were detected and were attributed to the raw materials. The increase in aluminum content resulted in a reduction of nitrogen in solid solution within the matrix due to the formation of aluminum nitride (AlN) at higher temperatures, altering the original composition of the alloy upon solidification. This led to changes in equilibrium diagrams when comparing the nominal composition (Fig. 4a–Table 2) with the real composition (Fig. 4b and the inserted table), exerting a pronounced effect on the final equilibrium phases and microstructure. Furthermore, when working with nitrogen content exceeding 0.4 wt%, during solidification, regions where the gaseous phase coexists with solid phases can emerge (as indicated in the red regions of the diagrams). This can lead to nitrogen loss through degassing, leading to the formation of voids in the alloy. The dashed line in the graph represents the solidification route of the alloy.

Lu et al. [17] conducted a study to investigate the formation of AlN inclusions in high-nitrogen steels with an approximate nitrogen content of 4000 ppm. Their research focused on the thermodynamics and kinetics of AlN precipitation, aiming at understanding the mechanisms underlying AlN inclusion formation and to establish a critical Al content below which the AlN formation in these steels is suppressed. The presence of these inclusions is closely associated with the aluminum (Al) content in the steel.

By their results, AlN inclusions start forming when the Al content exceeds 500 ppm, primarily in the liquid state of the steel. As the Al content decreases to values between 300 ppm and 500 ppm, the conditions for AlN formation are no longer met in the liquid state, thus

preventing their occurrence. However, during the solidification process, AlN inclusions may still appear when the concentrations of both Al and nitrogen (N) exceed the critical solubility of AlN due to an enrichment of N in the residual liquid. For Al contents ranging from 60 ppm to 300 ppm, the conditions for AlN formation are no longer met, leading to the absence of AlN inclusions during the solidification of the steel. Only a few small AlN inclusions may precipitate during the austenitization process. Furthermore, as the Al content decreases to 60 ppm, AlN inclusions are not observed in the austenitized samples. Therefore, to prevent AlN formation, the maximum allowable Al content is 60 ppm in steels with nitrogen contents around 0.4 wt%.

These findings are consistent with the results obtained in the present study, despite differences in alloy compositions. The alloy used in this work has Al and N contents of 0.16 and 0.44 in wt% (1600 and 4400 ppm), respectively, as shown in Fig. 4. (b), where AlN forms as the primary phase from the liquid. Despite these compositional differences, the results demonstrate that the presence of AlN inclusions is directly related to the Al content in the alloy. Hence, high nitrogen austenitic stainless steels are very sensitive to residual nitrogen, making then prone to readily form AlN precipitates in the first stages of solidification.

Another contaminant to be mentioned is sulfur. Since the manganese is a key element to improve the solubility of nitrogen and acting as austenitizing element, in presence of sulfur, manganese sulphide (MnS) is predicted, as shown in Fig. 4b. These inclusions are known to trigger pitting corrosion [18], and will have impact on the corrosion resistance of the alloy as will be discussed later.

The HTC method has proven to be a promising approach in the development of metal alloys with specific properties. The criteria established for screening allowed the selection of a promising alloy, accounting factors such as the temperatures of the σ and α phases, as well as the temperatures for carbide formation and austenite decomposition. The alloy met the recommended requirements for Cr, Ni, Mn, and Cu content, which are characteristics of the austenitic families [9].

3.2. Microstructural characterization

Fig. 5 presents the results of the synchrotron X-ray diffraction (SXRD) analysis of the recrystallized + water-quenched samples. The SXRD analysis of the samples revealed the predominant presence of the austenitic phase (γ), as indicated by the observed peaks. Additionally, less intense peaks corresponding to the AlN and MnS phases were identified. According to CALPHAD calculations, the volume fractions (vol%) of these phases were determined to be 0.44 vol% for AlN and 0.02 vol% for MnS. These results are in agreement with the theoretical expectations based on phase equilibrium diagrams for the system of interest, which reinforces the reliability of the analyses and the validity of the CALPHAD calculations performed. Furthermore, it is noteworthy that the steel is austenitic, as initially intended, demonstrating that the HTC method used in this work was successful in selecting the composition of this steel.

Fig. 6 shows the characteristic microstructure of HNSS in the recrystallized condition. As observed, the material exhibits an austenitic microstructure with the presence of annealing twins and AlN precipitates of various sizes within the grain interior and along grain boundaries. The AlN precipitates found in the material exhibit a wide range of shapes and can have various crystal structures. The most stable crystalline structure for AlN is hexagonal (space group P 63 mc) and the morphology of these precipitates can vary considerably depending on the alloying elements and their content added (especially Al and N), the applied heat treatment, and the material's processing history [19]. Consequently, AlN precipitates can appear as plates, needles, rectangular shapes, cubes, as well as finely dispersed spherical particles. In the austenitic region, the precipitation of AlN primarily occurs at grain boundaries given the significant volumetric incompatibility between the AlN precipitate and the steel matrix, as well as the enhanced diffusivity of elements at the grain boundaries compared to within the grains.

Fig. 7 shows the data obtained via EBSD analysis, with the most important information gathered from this analysis being the confirmation of AlN at both the grain boundaries and within the grains. Analyzing

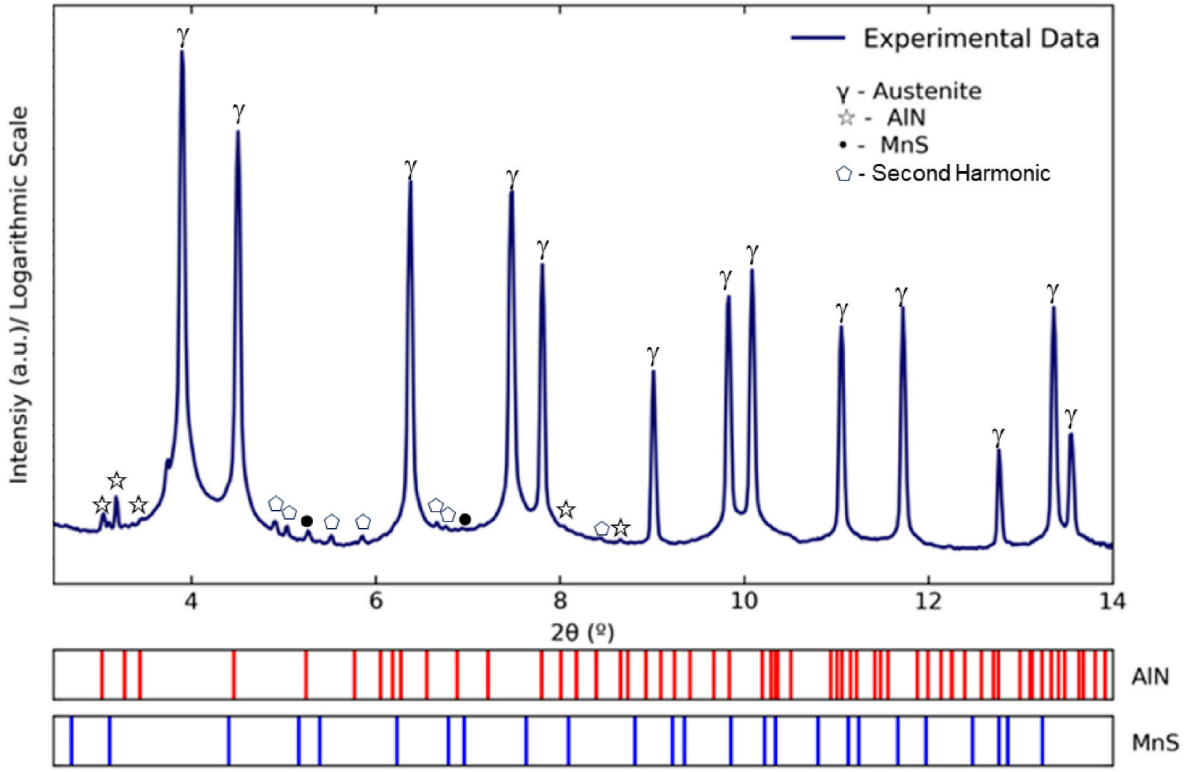

Fig. 5. Indexed SXRD diffraction pattern for the HNSS on the annealed + water quenched condition.

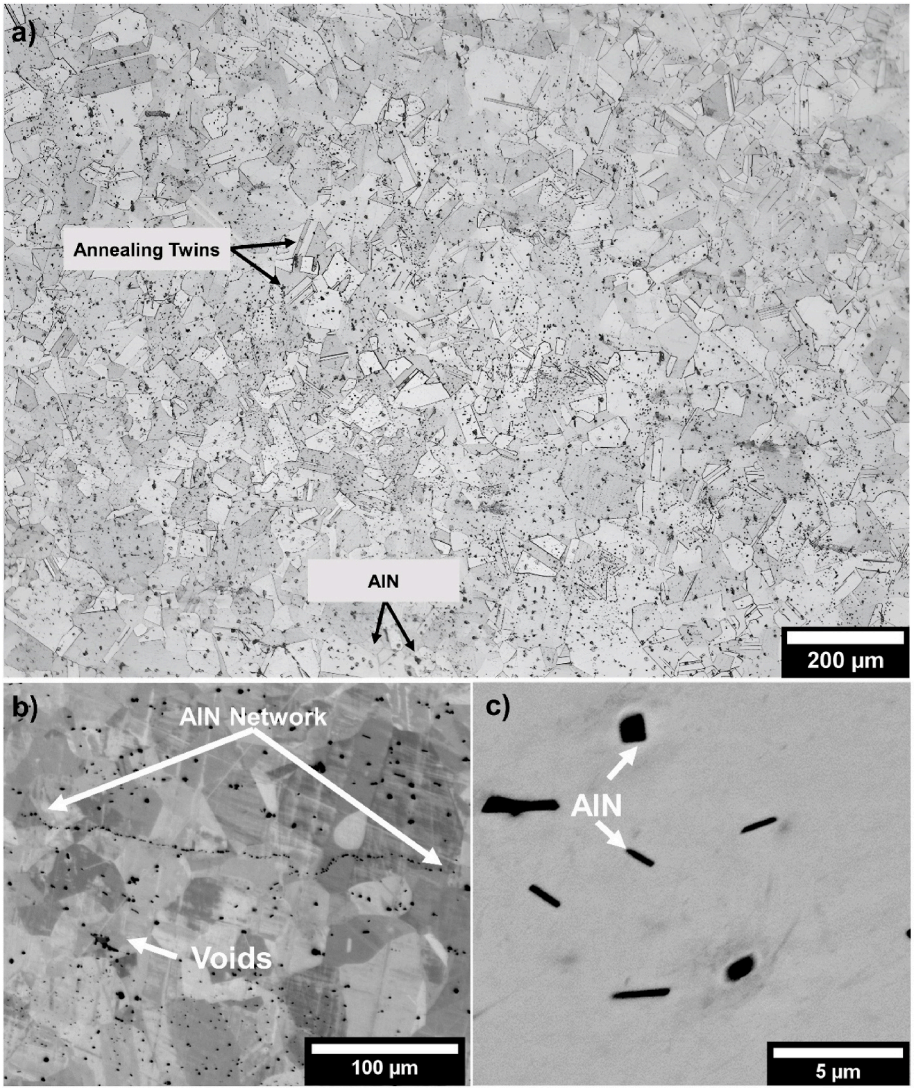

Fig. 6. a) Microstructure of HNSS obtained by optical microscopy, b) SEM-BSE micrographs showing AlN precipitates with different morphologies, c) Morphologies of AlN precipitates.

Fig. 7a, equiaxed grains with an average size of approximately 28 μm, measured using EBSD, along with AlN precipitates coexist, confirmed by EDS. In Fig. 7b, the inverse pole figure (IPF) reveals the absence of a preferred crystallographic orientation.

For a more detailed analysis of the precipitates, a TEM analysis of the sample under the same processing conditions was performed, as shown in Fig. 8. It is possible to observe that the AlN precipitates, with approximate sizes of 2 μm, are predominantly distributed along the grain boundaries of the austenite, thus confirming the previously discussed results. The diffraction pattern of an AlN precipitate is depicted in Fig. 8b along the [0 0 1] zone axis, displaying a hexagonal wurtzite-like structure. Additionally, Fig. 8c presents the results of EDS performed in TEM, where it was possible to observe the MnS inclusions, which were not previously detected by EDS in SEM.

3.3. Mechanical properties

The engineering stress–strain curves for HNSS, AISI 201 SS, and AISI 304 SS are presented in Fig. 9a. All steels exhibited continuous yielding followed by extensive strain hardening. From the analysis of the curves in Fig. 9a, it was observed that HNSS obtained the highest yield strength (σ_{ys}) and ultimate tensile strength (σ_{UTS}) values compared to AISI 201 SS and AISI 304 SS, but at the expense of the elongation at fracture (ε_f). This loss of ductility may be associated with the presence of AlN in the material, as pointed out by Ref. [19], who found that the precipitation of AlN within the grain interiors and at the grain boundaries of austenite directly affects the material's ductility. However, it should be noted that the HNSS yet displayed appreciable elongation of ~40%, given the quite refined and well distributed precipitates along the austenitic matrix.

The microstructure of the steel subjected to a solution treatment at 1150 °C reveals randomly oriented equiaxial austenite grains, with a few annealing twins, as depicted in Figs. 6 and 7. Furthermore, the high binding energy of nitrogen with dislocations results in a stronger effect of N on yield strength [20], reinforcing the values obtained in this work.

Rawers et al. [21] introduced an equation for solid-solution strengthening (σ_{ss}) by elemental N, **Eq. (1)**.

$$\sigma_{ys} = \sigma_0 + \alpha\,[N] + \beta\,[N]^{\frac{1}{2}} \quad (1)$$

Where [N] is the N concentration (wt%), the constant term (σ_0) in Eq. (1) represents the other strengthening contributions to yield strength for similar but nitrogen-free alloys. It decreases in importance as the temperature rises. The two terms (α and β) dependent on nitrogen concentration are associated with: (i) matrix strengthening due to dislocations interacting with interstitial nitrogen in the matrix and (ii) strengthening components due to dislocation drag, which results from nitrogen moving

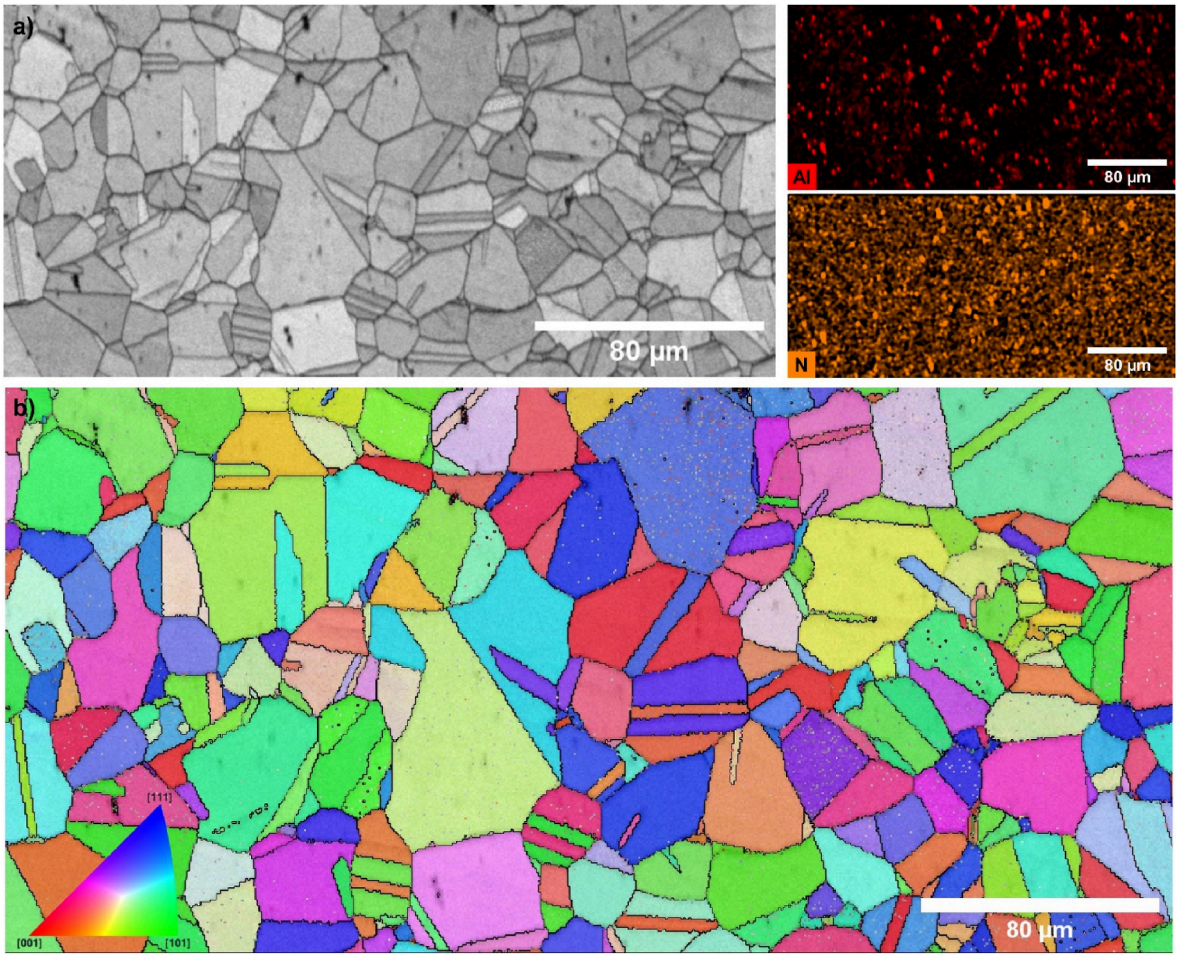

Fig. 7. EBSD maps and data for HNSS. a) SEM image and corresponding EDS for Al and N and b) grain size and grain distribution.

along with dislocations as they traverse the lattice.

At room temperature, σ_0, α, and β are 215 MPa, 939 MPa, and 61 MPa, respectively [21]. Note that the referenced article examined various compositions of FeCrMnNiN steels, with nitrogen content ranging from 0 to 1 in wt%. These values have been considered for our discussion, considering them as representative for this steel class. Considering that only 0.2 wt% of N is dissolved in the HNSS due to the formation of AlN, σ_{ss} is approximately 215 MPa. For AISI 201 SS and AISI 304 SS, which contain 0.16 wt% and 0.05 wt% of N, respectively, σ_{ss} values of approximately 174.6 MPa and 60.6 MPa were considered. Thus, the amount of interstitial nitrogen directly influences the yield strength attributed to solid solution strengthening, with nitrogen serving as an effective strengthener for stainless steel.

Fig. 9b shows the Vickers hardness values of the austenitic stainless steels used in this work. The HNSS presented the highest Vickers hardness values, reaching 304 HV, an increase of approximately 24.5% compared to AISI 201 and 71% compared to AISI 304. This indicates that HNSS has greater resistance to localized plastic deformation, which is reflected in higher hardness. Besides nitrogen as an effective solid solution strengthener, the AIN is regarded as a hard reinforcement (1224 HV, [22]), especially when refined and homogeneously distributed along the stainless steel matrix.

The 2XX stainless steel class is prone to martensitic transformation upon deformation, which means their austenite is metastable. This characteristic allows these steels to have a high work-hardening capacity, thanks to the TRIP effect, resulting in excellent energy absorption capability. To investigate and observe the TRIP effect, an *in-situ* tensile test was conducted to determine whether the steel can undergo martensitic transformation during mechanical stress, resulting in a significant increase in its work-hardening and energy absorption capacity.

Through the analysis of Fig. 10a and b, during the *in-situ* tensile experiment, the martensitic phase was absent, and thus, no TRIP effect was detected. Instead, only the broadening of the diffraction peaks was observed (Fig. 10c), indicating the increase in dislocation density, a normal material ductile response along deformation. Thus, the austenite of HNSS has relatively high stability, suggesting that there may be room to further reducing the nickel or manganese content.

3.4. Corrosion behavior

DL-EPR, Fig. 11a, was employed to qualitatively assess the degree of sensitization. The I_r/I_a ratio values (%) obtained from the DL-EPR curves are summarized in the inserted Table in Fig. 11a with the interpretation according to the ISO 12732. All samples revealed I_r/I_a below 1%, indication of unsensitized microstructure.

During the activation polarization, the AISI 201 SS requires a higher charge (area under the activation curve) and peak current density (I_a) before effective passivation, characterized by a steep drop in current density. This fact indicates a greater difficulty in forming the passive film for AISI 201 SS, followed by AISI 304 SS, although it requires a lower charge and I_a. On the other hand, HNSS is characterized by the lowest charge and I_a required before achieving an effective passivation during the activation scan, which occurs at considerably lower potentials than AISI 201 SS and 304 (see arrows in Fig. 11a). HNSS has higher Cu and N contents compared to the other two steels, which may provide a possible explanation for this observed phenomenon. The increase in

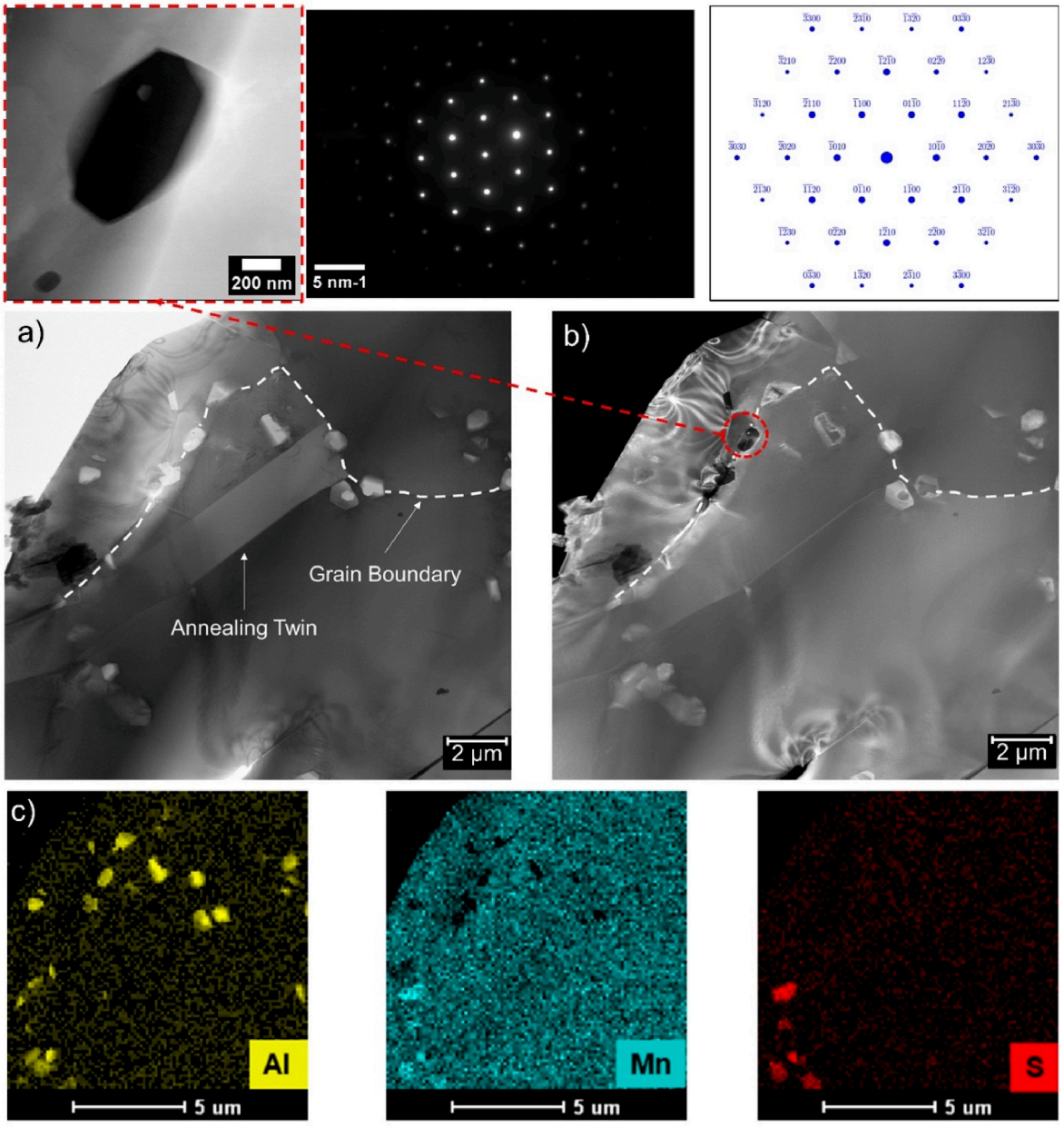

Fig. 8. Bright-field (a) and dark-field (b) images for the HNSS with the diffraction pattern of the AlN, alongside TEM EDS in (c), showing the MnS inclusions.

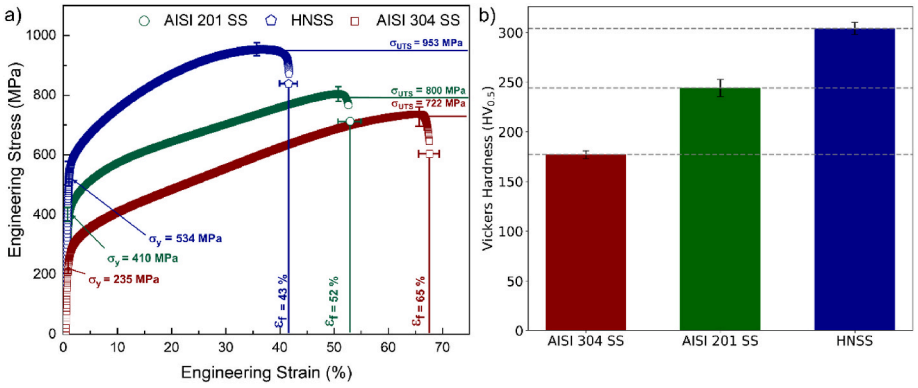

Fig. 9. a) Engineering stress-strain curves and b) Vickers hardness for the austenitic stainless steels HNSS, 201, and 304.

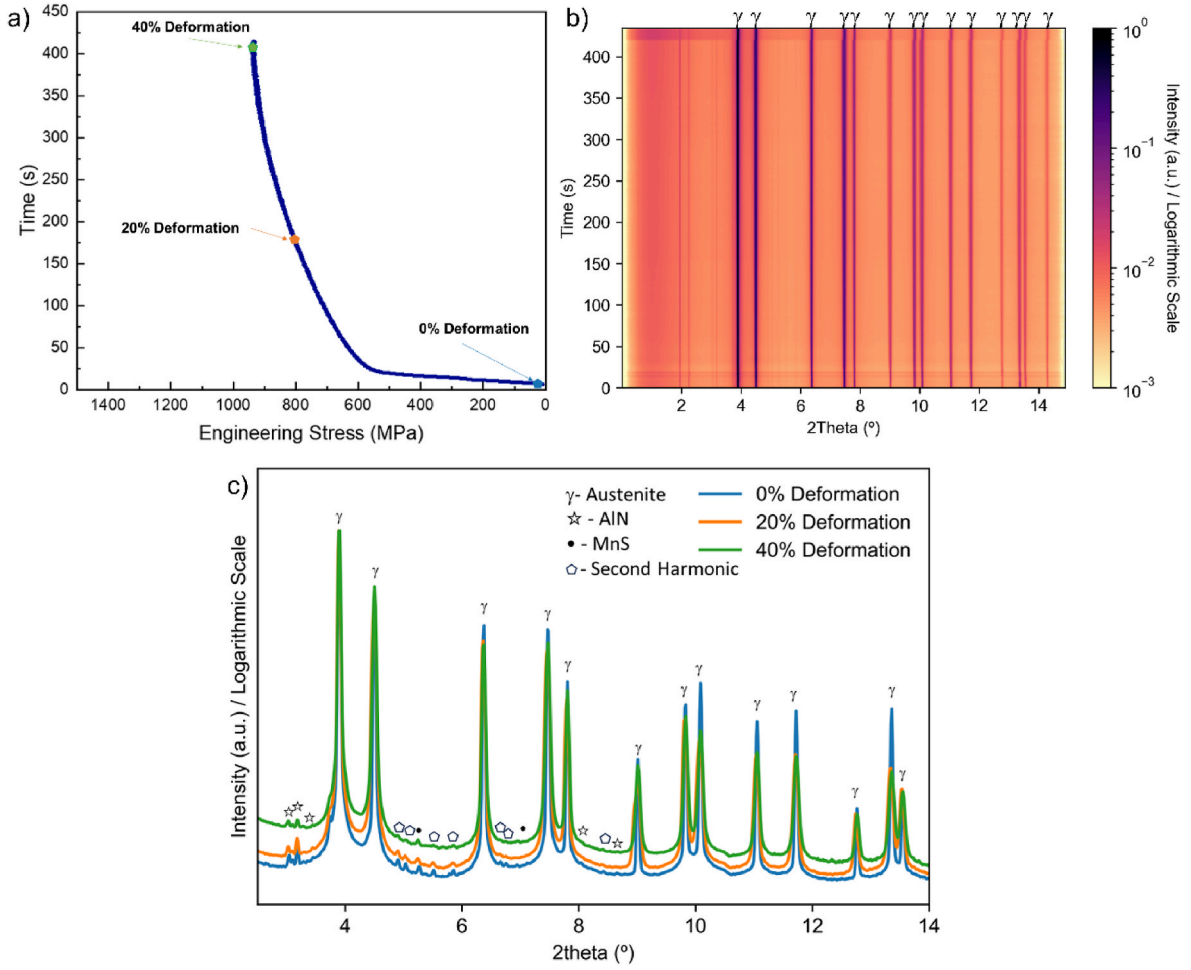

Fig. 10. a) Engineering stress curve as a function of time, b) SXRD during tensile testing of the sample and c) SXRD during different deformation stages of the in-situ tensile test.

these elements in the composition can influence on the early formation of the passive film during polarization with easer active-to-passive transition, resulting in a lower charge and I_a required for effective passivation [23]. This difference in chemical composition can play a significant role in corrosion resistance and the (re)formation of the protective film, thus influencing the electrochemical behavior of HNSS compared to AISI 201 SS and 304 SS.

During the reactivation scan, only the AISI 304 SS exhibited a reactivation peak albeit much inferior than its activation peak. AISI 201 SS had the lowest values for the I_r/I_a ratio, as expected since it did not undergo the heat treatment steps that AISI 304 SS and HNSS went through. It is important to note that all values obtained for the I_r/I_a ratio are below the limits established for non-sensitized materials (<1%) [14]. This indicates that there was no sensitization in the material.

The DL-EPR test is a sensitive technique capable of detecting variations in material reactivity. However, the interpretation of the results should consider the specific context and consider other complementary analyses for a comprehensive assessment of sensitization and, therefore, on the susceptibility to intergranular corrosion. Micrographs after the electrolytic oxalic acid etch test on HNSS, AISI 201 SS, and AISI 304 SS were used, Fig. 11b, as a complement to the results assessed from DL-EPR (Fig. 11a). The microstructure of all steels in Fig. 11b was free from intergranular attack, with a step structure along the grain boundary, indication of unsuspected microstructure, which agrees with the DL-EPR results of all samples (Fig. 11b). Thus, the microstructures of these steels are unsensitized and not susceptible to intergranular corrosion.

Fig. 12 displays the polarization curves in 3.5% NaCl solution for the stainless steels with the electrochemical parameters obtained from the polarization curves. The overall behavior of all stainless steel is similar, with comparable E_{corr} and clear passivation window upon anodic polarization. However, the AISI 304 SS and AISI 201 have a more stable passive region compared to HNSS, which exhibits a more unstable curve characterized by fast spikes of current density. This instability is a characteristic feature of the nucleation and subsequent repassivation of meta-stable pits. This behavior may be related to the material having a more heterogeneous surface, resulting in a non-uniform distribution of current and ion flow during the corrosion process. The similarity in behavior of HNSS steel to AISI 201 SS, as well as the instability in the polarization curves exhibited by HNSS steel, may be directly linked to these steels having a higher Mn content when compared to AISI 304 SS. Consequently, with an increase in Mn content, the corrosion current (I_{corr}) increases, while the E_{corr} decreases, signifying compromised corrosion resistance in the presence of higher Mn content [24]. Additionally, the presence of precipitates within and along grain boundaries directly affects the material's corrosion behavior, as these precipitates can serve as nucleation sites for pit formation. Park, K. & Kwon, H. (2010) [25] research revealed a significant increase in the nucleation and repassivation of metastable pits with higher Mn content. This can be attributed to the formation of non-metallic inclusions, such as oxides, which act as initiation sites for pit formation. Additionally, the increased pit activity can be linked to the higher reactivity of Mn compared to other alloying elements.

Remarkably, only HNSS demonstrated the potential for repassivation (E_{rp}) during reverse polarization albeit very close to E_{corr}. Despite

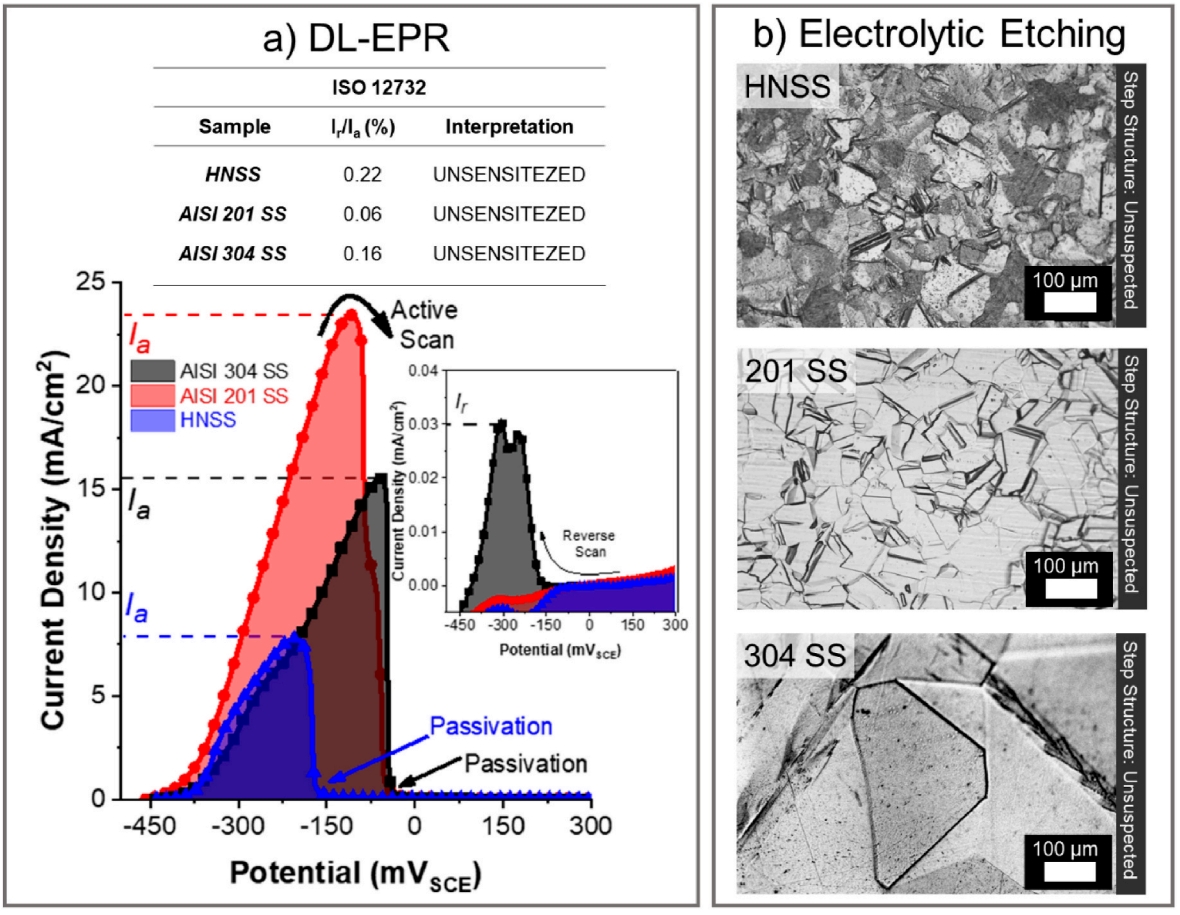

Fig. 11. a) DL-EPR curves and the degree of sensitization, I_r/I_a (%), and the general interpretation according to the [14]. b) Susceptibility of intergranular corrosion following the oxalic electrolytic etching, Practice A, according to the [15].

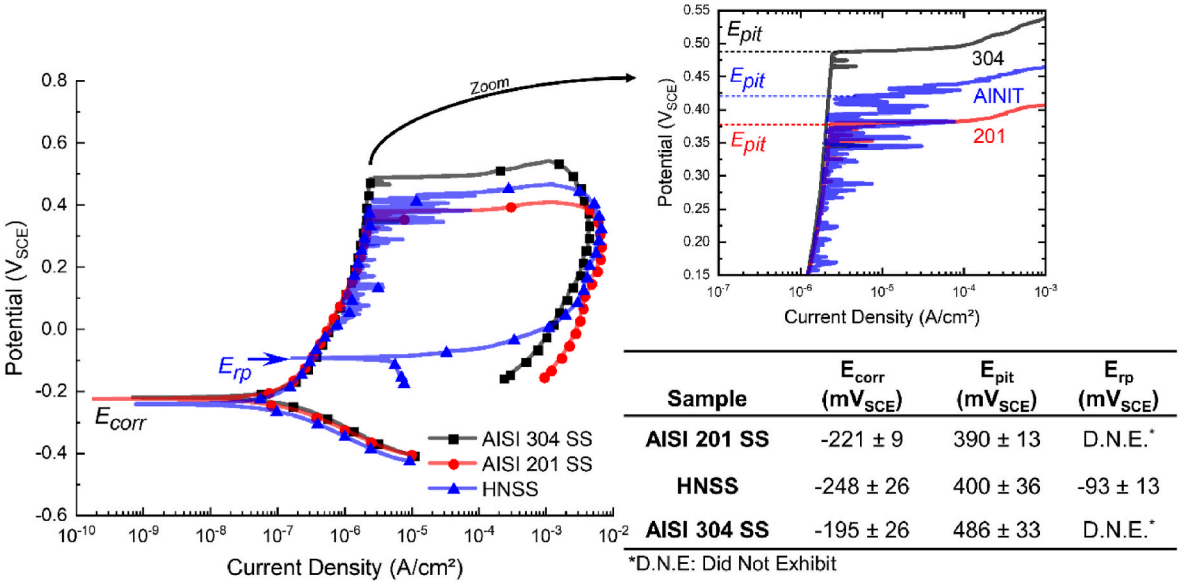

Sample	E_{corr} (mV$_{SCE}$)	E_{pit} (mV$_{SCE}$)	E_{rp} (mV$_{SCE}$)
AISI 201 SS	-221 ± 9	390 ± 13	D.N.E.*
HNSS	-248 ± 26	400 ± 36	-93 ± 13
AISI 304 SS	-195 ± 26	486 ± 33	D.N.E.*

*D.N.E: Did Not Exhibit

Fig. 12. Representative potentiodynamic polarization curves in 3.5% NaCl solution for the stainless alloys.

exhibiting metastable pits during anodic polarization and even at a degradation level of 1 mA cm^{-2}, as for the AISI 304 SS and AISI 201 SS, only HNSS was able to halt pit propagation. This can be attributed to the residual N content in solid solution. Nitrogen in solid solution within the steel works to elevate the steel's potential, making it more favorable for repassivation [2]. Its presence as a solid solution reinforces the repassivation process, enhancing the material's ability to form and regenerate the protective passive film due to its interactions with H^+ ions and its capacity to counteract the pH decrease caused by hydration. During pit formation, the hydration of dissolved cations increases the acidity

within the pit by forming solvated H^+ ions. However, nitrogen reacts with these H^+ ions, contributing to the formation of compounds such as NH_3 and NH_4^+. This reaction helps raise the pH value within the pit, reducing acidity, and consequently facilitating the repassivation process [3]. Indeed, N-alloying is a promising approach to improve the corrosion resistance of alloys, including high-entropy alloys (HEA) [26]. Besides alleviating the acidification of the surface, thus accelerating the deposition of protective oxygen-rich Cr compounds, the passive film nucleation and growth are enhanced, ensuring a less detective coveting of the surface.

Fig. 13 presents the EIS data of the stainless steels. The Nyquist plots of all alloys, Fig. 13a and b, are characterized by a truncated semi-circle typical of RC behavior. The Bode phase plots, Fig. 13c and d, exhibit an enlarged but single phase peak, and the Bode IZI plots, Fig. 13e and f, display, at the lowest probed frequency of 10 mHz, IZI > 10^5 Ω cm^2. The EIS response of all tested stainless steel was similar, and characteristic of passivated alloys.

Two approaches were used to analyze the experimental EIS data. First, an electrical equivalent circuit (EEC) using the Randle's analog was considered. Indeed, Engelhardt et al. [27] have shown that highly

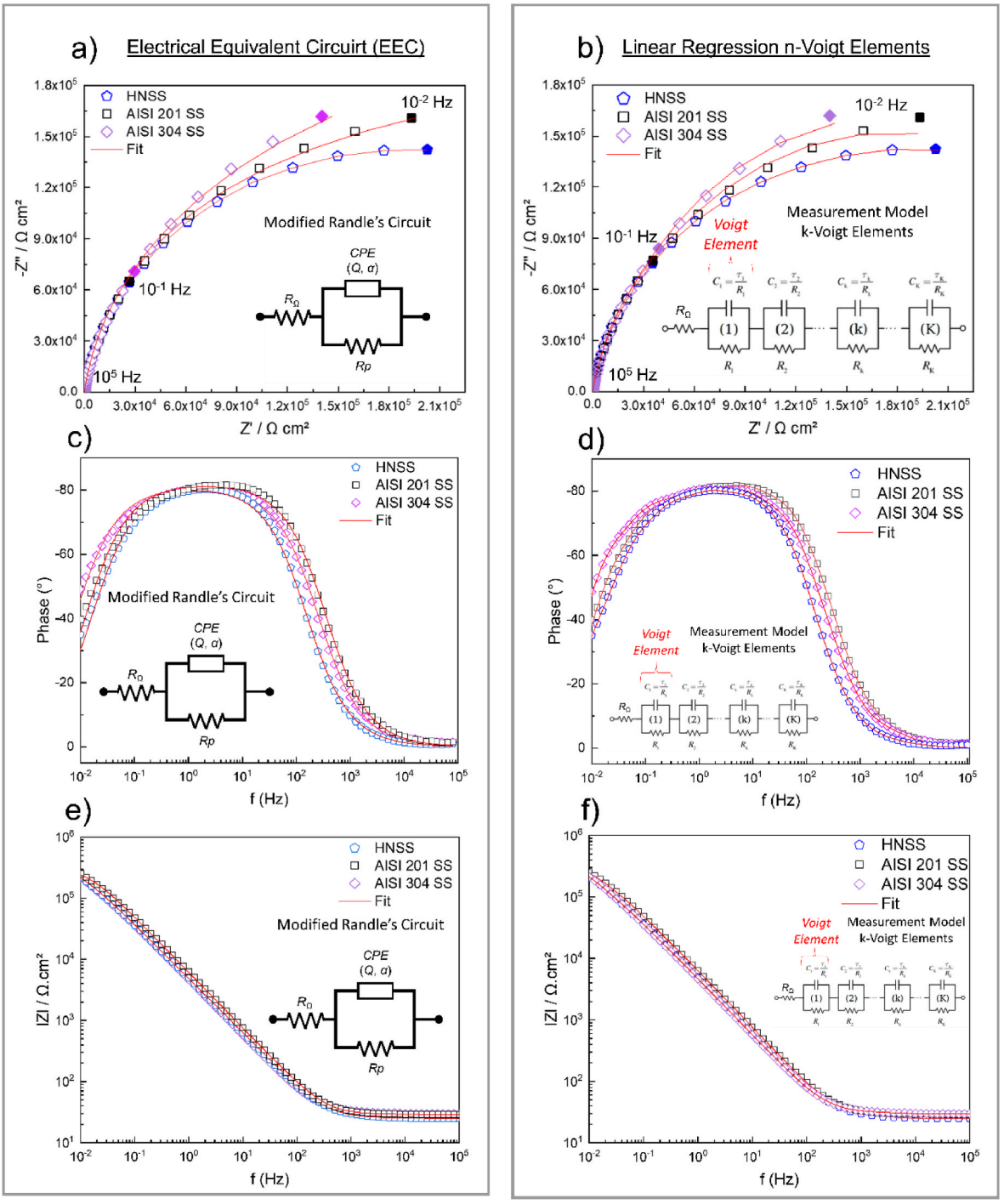

Fig. 13. Impedance data of the stainless steels with different data treatment. a) Nyquist diagrams, and Bode phase (d) and Bode IZI plots with fitting from electrical equivalent circuit (EEC) approach using a Modified Randle's analog. a) Nyquist diagrams, and Bode phase (d) and Bode IZI plots with fitting from linear regression approach using the Measurement Model with 07-Voigt elements.

passivated alloys may display a single time constant, where a simple resistor in series with a parallel arrangement of a resistance and a capacitor (or a constant phase element, CPE) adequately describes the EIS data. The inset model in Fig. 13a–c,e is therefore deemed as representative of the properties of the overall interface, where R_Ω is the ohmic resistance, the R_p is the polarization resistance, and the CPE is the constant phase element to account the capacitance-like response from the whole interface, being the CPE characterized by its parameter (Q) and coefficient (α).

Table 3 summarizes the ensemble of the values of the parameters from fitting the EIS of the Randle's analog to the experimental EIS data. The R_p values ranged from 270 to 320 kΩ cm^2 and, considering the deviations, are all comparable regardless of the stainless steels. Thus, at AC perturbation around rest, all alloys exhibit appreciable polarization resistance, an indication of comparable corrosion behavior. Also, the values of α ~0.9, i.e. close to 1.0, pointed out to the capacitive-like response from the surface and, the similar values among stainless steels of Q (33–46 μF s$^{\alpha-1}$ cm^{-2}), suggest similarity from the capacitive response that could be related to the passive film formed.

The EEC approach assumes that the passive film is homogeneous in a plane parallel to the sample surface, which is a simplifying but useful hypothesis for comparative purposes. Note that several precipitates such as AIN and MnS have been found in HNSS (Figs. 5–8). To further investigate the EIS data, a linear regression approach by using the Measurement Model has been considered, allowing to assess the mean properties in a plane parallel to the surface, however, considering the heterogeneities in the direction normal to the sample surface. This constitutes an interesting first approach for the HNSS steel which has not been studied until now to extract more reliable resistive and capacitive results of the corroding system based on stainless steel [28].

Table 3 details the values of the parameters from considering a linear regression with 7 Voigt elements to the experimental EIS data using the Measurement Model approach. Both R_Ω and R_p trend and values (266–310 kΩ cm^2) agree quite well to the results from EEC analyses (270–320 kΩ cm^2). However, the linear regression allowed to extract values of effective capacitance, C_{eff}, where the values are similar to all tested stainless steels, and in the range of 10–13 μF cm^{-2}, typical of what would be expected to nanometric passive film on austenitic stainless steels from EIS data treatment [29].

Thus, the ensemble of the electrochemical results pointed out that HNSS developed was unsensitized (Fig. 11a) and not suspect after passing to risk of intergranular corrosion trial (Fig. 11b). At rest under small AC perturbation, the electrochemical responses of HNSS were similar to that of AISI 304 and 201 SSs, with characteristic values of R_p and C_{eff} that agree to austenitic stainless steels in the passive state (Fig. 13, Table 3). Finally, cyclic potentiodynamic polarization indicated that HNSS display an enlarged passivation plateau upon anodic polarization and a pitting potential that even surpass that of AISI 201 SS. However, given the presence of precipitates such as AIN and MnS, the occurrence of metastable pitting was more evident in the HNSS (Fig. 12).

Table 3
Ensemble of fitting: i) using the Randle's electrical equivalent circuit (ECC) analog to model the experimental EIS data, and ii) from linear regression using the Measurement Model approach considering n-Voigt elements consisting of a resistor in parallel with a capacitor. Values presented as mean values and their standard deviation for analyses in triplicate.

Electrical Equivalent Circuit Approach [Randle's Model]					
Sample	R_Ω (Ω·cm^2)	R_p (kΩ·cm^2)	Q (μF s$^{\alpha-1}$ cm^{-2})	α	χ^2 (10^{-3})
304 SS	26 ± 4	280 ± 74	46 ± 5	0.909 ± 0.007	1.0 ± 0.7
201 SS	27 ± 2	270 ± 53	33 ± 2	0.914 ± 0.002	1.1 ± 0.3
HNSS	28 ± 3	320 ± 56	36 ± 10	0.898 ± 0.008	0.6 ± 0.1
Linear Regression Approach [Measurement Model, n-Voigt Elements]					
Sample	R_Ω (Ω·cm^2)	R_p (kΩ·cm^2)	C_{eff} (μF·cm^{-2})	Voigt Number	χ^2 (10^{-3})
304 SS	25 ± 4	266 ± 68	13 ± 3	7	26 ± 2
201 SS	27 ± 2	274 ± 50	11 ± 1	7	19 ± 1
HNSS	28 ± 3	310 ± 85	10 ± 2	7	7 ± 1

4. Lesson learned

Development and processing of high nitrogen stainless steels can be challenging, requiring a deep understanding of the reactivity of elements and stability of phases during casting, thermomecanical processing and heat treatment. The challenges of microstructural control arise from several pitfalls, such as those the authors have encountered in their own work, which have been discussed together with others reported in the literature.

This section aims to clarify and discuss how to avoid potential risks such as degassing and formation of deleterious phases. At the end, it is also pointed out some opportunities to further explore: a) the synergetic effect of nitrogen and molybdenum to improve the resistance against pitting corrosion, and b) decrease the austenitizing elements, such as nickel or manganese, since the austenite obtained for HNSS has relatively high stability, as evidenced by the absence of the TRIP effect in the in-situ tensile test, and/or increase ferritizing elements such as chromium and molybdenum to achieve a stable austenitic matrix with increased nitrogen solubility and improved corrosion resistance of the alloy.

From Fig. 14, calculated from the nominal composition of HNSS detailed in Table 2, the isopleth diagram highlights the strict and narrow control for ensuring nitrogen in solid solution. Starting from the melting, excessive overheating causes nitrogen loss through degassing from the liquid for temperatures superior to 1526 °C ($T_{liq.degass}$) this, besides nitrogen loss, may cause large pores. Given the liquidus temperature ($T_{liquidus}$) of 1378 °C, the allowable temperature range ($T_{liq.degass} - T_{liquidus}$) during melting is 148 °C. Note that for casting, the overheating applied to ensure mold filling between 100 and 150 °C falls very close to the allowed temperature range. This implies the need for careful control of the casting temperature and the temperature of the mold to avoid premature freezing and incomplete filling, giving that the solidification interval is also narrow (ΔT = 50 °C).

An interval of 189 °C of a single FCC phase exists between 1328 °C and 1140 °C, which is appropriate for hot rolling. This interval is followed by the precipitation of chromium nitride, Cr_2N, from the FCC phase, wich poses a risk of formation of a Cr-depleted region and reducing the amount of nitrogen in solid solution. Thus, rapid solidification from the single FCC range is mandatory to suppress the Cr_2N formation, whether from hot rolling of recrystallization heat treatment of cold rolled microstructure.

The maximum nitrogen content, 0.46 wt%, in solid solution is dictated by the alloy composition and represented graphically by the "nose" of the FCC + GAS field. Even if superior nitrogen content dissolved into the molten is permissible, during the solidification solid state degassing would occur. Since nitrogen is a strong austenitizing alloying element, is decrease below 0.39 wt% would destabilize partially the FCC into BCC, resulting into the duplex field.

Certain impurities also significantly compromise the processability and corrosion resistance attributed of N- and Mn-containing stainless steels, as illustrated in Fig. 15. Traces of aluminum superior to 100 ppm already cause the formation of AlN, which is formed at high temperature from the liquid, and remains stable upon solidification, and therefore, it is not eliminated by solubilizing heat treatment. AlN tends to concentrate within the grain boundaries, with risk of cracking during thermomechanical deformation, resulting in a deformed steel with the appearance of "rock candy". Thus, the maximum Al threshold from precursor should not exceed 100 ppm for the alloy of this study. Other strategies exist to mitigate the deleterious effect of AlN precipitates in

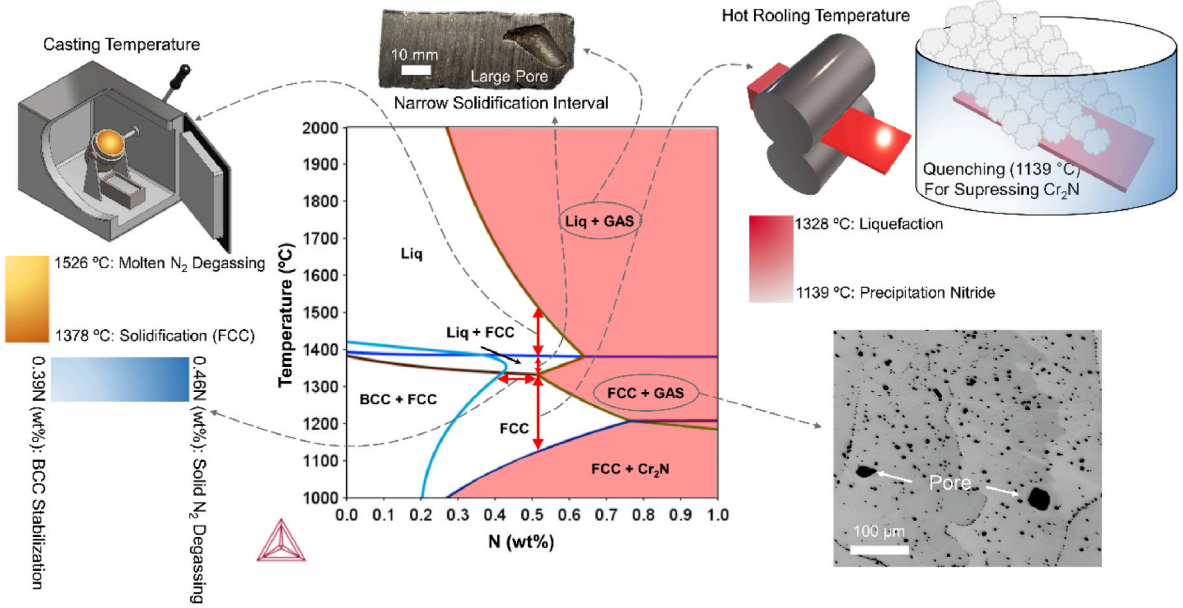

Fig. 14. Pitfalls during processing high nitrogen stainless steels using as example the alloy of this work, HNSS Nominal, Table 1.

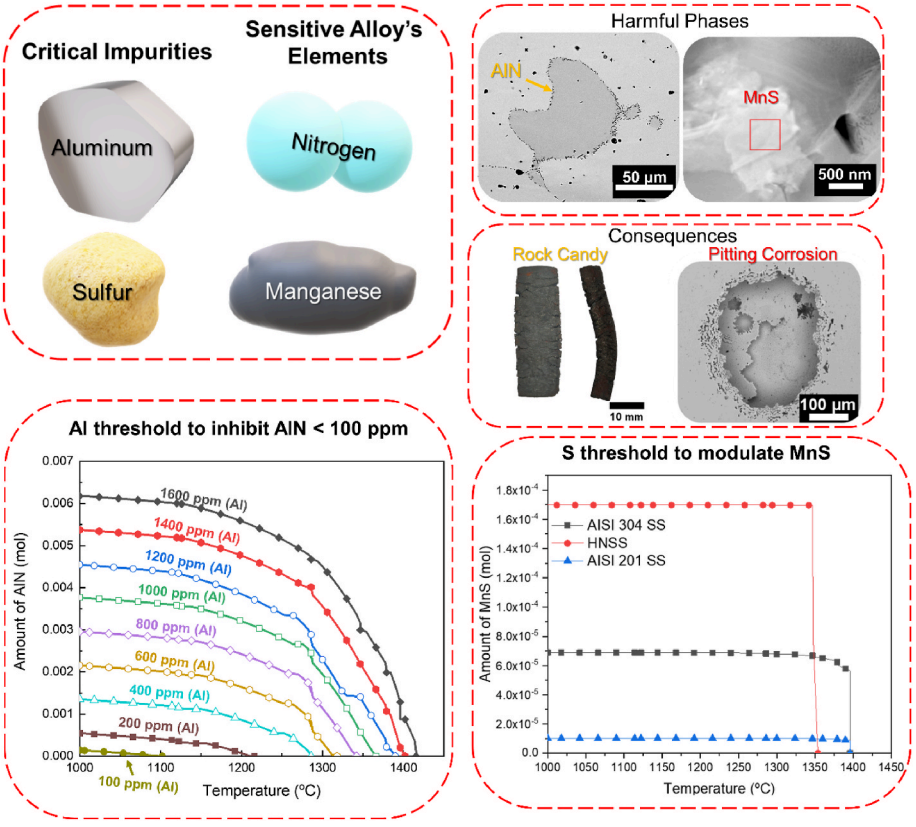

Fig. 15. Effect of impurities on the high nitrogen stainless steels, causing deviation of the nominal composition, HNSS Nominal (Table 2) to Fig. 4b and inserted Table.

high nitrogen steels, aiming to reduce the elevated cost associated with precursors for steelmaker with stringent Al contaminations [30]. Appreciable plastic deformation is achieved by activating the stacking faults in nano-sized AlN, such as during martensitic transformation upon quenching, paving the way for additional strategies to widen the Al contamination tolerance and broadening the processing window of HNSS.

Sulfur is also recognized to be an impurity to be minimized in stainless steel, especially for those containing appreciable content of manganese. The main risk is the excessive formation of manganese sulfite, MnS, regarded to be locations for triggering pitting corrosion. According to the [9], the maximum sulfur content is 300 ppm for both 304 and 201 stainless steels. All alloys evaluated presented sulfur content below 300 ppm. However, among the alloys investigated, the HNSS

exhibited the highest fraction of MnS, as indicated by the thermodynamic calculations in Fig. 15. Metastable pitting occurrence was seen for both 304 and 201 stainless steels, and ascribed to the MnS, albeit in reduced content. Besides the MnS, given the high frequency of occurrence of metastable pitting corrosion for HNSS, the AlN is a potential site for weaker passive film stability. The large extent of metastable pitting along anodic polarization before active pitting corrosion could be ascribed to the inhibitory role of nitrogen in solid solution even in presence of MnS and AlN, which hinders the propagation of pits, and assist the healing of the surface.

Fig. 10 showed the high-energy synchrotron X-ray diffraction experiment under tensile condition. Austenite remained stable even after 40% of elongation, with no occurrence of martensite given the high austenite stability. This could indicate that austenitic elements such as manganese, which impairs the corrosion resistance, could be reduced. Also, this opens opportunities to further increase the addition of ferritizing elements such as molybdenum and, still, ensuring single austenitic alloy. It has been reported the synergistic effect of nitrogen and molybdenum for enhancing the resistance against pitting corrosion.

High nitrogen stainless steels have more potential than has yet been revealed. Novel computational tools open opportunities on the conception of new alloy composition assisted by thermodynamic calculations and high-throughput screening strategies, exploring a vast compositional field. Besides pointing out promising alloy composition, the computational methods and screening allow also to count the aspects such as raw material cost, pitting resistance equivalent number, processability characteristics, and impurity tolerance. All these valuable information give a guideline to the alloy with better portfolio of cost, processability and properties that of course must be validated by experimentation.

5. Conclusion

- The approach of designing high-N austenitic stainless steels using the CALPHAD method proved promising, resulting in steel with an austenitic microstructure after heat treatments, and the absence of the TRIP effect in the HNSS steel suggests nitrogen's influence in stabilizing the austenite phase, which reduces the tendency to form stress-induced martensite.
- Due to impurities from the raw material, the alloy exhibited high levels of Al, resulting in a reduction in the amount of N in the solid solution due to the formation of aluminum nitride as the primary phase. Nevertheless, the HNSS alloy proposed in this study showed the highest yield strength and tensile strength values, 534 MPa and 953 MPa, respectively. Despite the reduction in elongation caused by AlN, HNSS still presented ~40% elongation.
- The developed HNSS exhibited excellent resistance to sensitization and demonstrated corrosion behavior similar to AISI 201 SS in a 3.5% NaCl solution, despite showing more prominent metastable pitting due to the presence of precipitates such as AIN and MnS. Nevertheless, it was the only material capable of repassivating after pit nucleation. Furthermore, in both EIS approaches used in this work - utilizing the EEC method and through linear regression with measurement model software - it was observed that HNSS exhibited behavior similar to AISI 304 and AISI 201 steels. This indicates the presence of a dense and resistant passive film, as evidenced by its α value of approximately 0.9, representing a capacitive-like response from the surface, and characteristic values of R_p and C_{eff} consistent with austenitic stainless steels in the passive state.
- Several pitfalls and challenges for developing and processing high nitrogen stainless steels have been discussed aiming to avoid several typical problems, such as: i) solid and liquid degassing and ii) formation of harmful precipitates, and how they dictate the properties and processability.

Data availability

The data that support the findings of this study are available on request from the corresponding author.

Declaration of competing interest

The authors declare that they have no known competing financial interests or personal relationships that could have appeared to influence the work reported in this paper.

Acknowledgments

This study was financed in part by the Coordenação de Aperfeiçoamento de Pessoal de Nível Superior - Brasil (CAPES) - Finance Code 001. V.H.M.M. Ferreira is grateful for the support of the Brazilian National Council for Scientific and Technological Development (CNPq) (grant number 131330/2021-7). G.Y. Koga thanks the financial support of CNPq (Universal Project, grant number 407651/2021-7). F.G.C. acknowledges the financial support from FAPESP, grant 2022/02770-7. Research was sponsored by the Army Research Office and was accomplished under Grant Number W911NF-23-1-0310. The views and conclusions contained in this document are those of the authors and should not be interpreted as representing the official policies, either expressed or implied, of the Army Research Office or the U.S. Government. The U. S. Government is authorized to reproduce and distribute reprints for Government purposes notwithstanding any copyright notation herein. The authors are also grateful for the electron microscopy facilities from the Laboratory of Structural Characterization of the Federal University of São Carlos (LCE/DEMa/UFSCar), and the overall facilities and staff of the Center for Development and Characterization of Material of the Federal University of São Carlos (CCDM/DEMa/UFSCar). The authors are grateful for the 201 and 304 stainless steels provided by Aperam South America.

References

[1] Ping Lang Y, peng Qu H, tao Chen H, qing Weng Y. Research progress and development tendency of nitrogen-alloyed austenitic stainless steels. J Iron Steel Res Int 2015;22:91–8. https://doi.org/10.1016/S1006-706X(15)60015-2.
[2] Baba H, Kodama T, Katada Y. Role of nitrogen on the corrosion behavior of austenitic stainless steels. Corros Sci 2002;44:2393–407. https://doi.org/10.1016/S0010-938X(02)00040-9.
[3] Olefjord I, Wegrelius L. The influence of nitrogen on the passivation of stainless steels. Corros Sci 1996;38:1203–20. https://doi.org/10.1016/0010-938X(96)00018-2.
[4] Speidel MO. Nitrogen containing austenitic stainless steels. Materwiss Werksttech 2006;37:875–80. https://doi.org/10.1002/mawe.200600068.
[5] Stein G, Hucklenbroich I. Manufacturing and applications of high nitrogen steels. Mater Manuf Process 2004;19:7–17. https://doi.org/10.1081/AMP-120027494.
[6] Zhang S, Wang Q, Yang R, Dong C. Composition equivalents of stainless steels understood via gamma stabilizing efficiency. Sci Rep 2021;11:5423. https://doi.org/10.1038/s41598-021-84917-z.
[7] Kattner RU, Kattner RU. The CALPHAD method and its role in material and process development. Tecnol Em Metal Mater e Mineração 2016;13:3–15. https://doi.org/10.4322/2176-1523.1059.
[8] Moon J, Lee T-H, Shin J-H, Lee J-W. Hot working behavior of a nitrogen-alloyed Fe–18Mn–18Cr–N austenitic stainless steel. Mater Sci Eng A 2014;594:302–8. https://doi.org/10.1016/j.msea.2013.11.090.
[9] ASTM A240/A240M-22 - Standard Specification for chromium and chromium-nickel stainless steel plate, sheet, and strip for pressure vessels and for general applications.
[10] Jargelius-Pettersson RFA. Application of the pitting resistance equivalent concept to some highly alloyed austenitic stainless steels. Corrosion 1998;54:162–8. https://doi.org/10.5006/1.3284840.
[11] Craig B. Clarifying the applicability of PREN equations: a short focused review. Corrosion 2021;77:382–5. https://doi.org/10.5006/3723.
[12] Daily Metal Price:Free Metal Price Tables and Charts. https://www.dailymetalprice.com/(accessed November 14, 2023)..
[13] ASTM International. ASTM E407-07e1: standard practice for microetching metals and alloys. vol. PA. 2007.
[14] ISO 12732. Corrosion of metals and alloys — electrochemical potentiokinetic reactivation measurement using the double loop method (based on Cihal's method). 2006.

[15] ASTM International. Detecting susceptibility to intergranular attack in austenitic stainless steels. 1985.
[16] Watson W, Orazem ME. EIS: measurement model program program. ECSarXiv; 2023. https://doi.org/10.1149/osf.io/kze9x., Version 1.8.
[17] Lu P-C, Li H-B, Feng H, Jiang Z-H, Zhu H-C, Liu Z-Z, et al. Formation mechanism of AlN inclusion in high-nitrogen stainless bearing steels. Metall Mater Trans B 2021; 52:2210–23. https://doi.org/10.1007/s11663-021-02171-0.
[18] Ryan MP, Williams DE, Chater RJ, Hutton BM, McPhail DS. Why stainless steel corrodes. Nature 2002;415:770–4. https://doi.org/10.1038/415770a.
[19] Wilson FG, Gladman T. Aluminium nitride in steel. 33:221–86, https://doi.org/10.1179/IMR.1988.33.1.221; 2013.
[20] Saenarjhan N, Kang J-H, Kim S-J. Effects of carbon and nitrogen on austenite stability and tensile deformation behavior of 15Cr-15Mn-4Ni based austenitic stainless steels. Mater Sci Eng A 2019;742:608–16. https://doi.org/10.1016/j.msea.2018.11.048.
[21] Rawers J, Grujicic M. Effects of metal composition and temperature on the yield strength of nitrogen strengthened stainless steels. Mater Sci Eng A 1996;207: 188–94. https://doi.org/10.1016/0921-5093(95)10031-8.
[22] Baik Y, Drew RAL. Aluminum nitride: processing and applications. Key Eng Mater 1996;122–124:553. https://doi.org/10.4028/WWW.SCIENTIFIC.NET/KEM.122-124.553.
[23] Sedriks AJ. Corrosion of stainless steelvol. 2. Other Inf PBD 1996; 1996. Medium: X; Size: [200] p.
[24] Zhang YS, Zhu XM, Zhong SH. Effect of alloying elements on the electrochemical polarization behavior and passive film of Fe–Mn base alloys in various aqueous solutions. Corros Sci 2004;46:853–76. https://doi.org/10.1016/J.CORSCI.2003.09.002.
[25] Park KJ, Kwon HS. Effects of Mn on the localized corrosion behavior of Fe–18Cr alloys. Electrochim Acta 2010;55:3421–7. https://doi.org/10.1016/J.ELECTACTA.2010.01.006.
[26] Feng H, Li H-B, Dai J, Han Y, Qu J-D, Jiang Z-H, et al. Why CoCrFeMnNi HEA could not passivate in chloride solution? – a novel strategy to significantly improve corrosion resistance of CoCrFeMnNi HEA by N-alloying. Corros Sci 2022;204: 110396. https://doi.org/10.1016/j.corsci.2022.110396.
[27] Engelhardt GR, Case RP, Macdonald DD. Electrochemical impedance spectroscopy optimization on passive metals. J Electrochem Soc 2016;163:C470–6. https://doi.org/10.1149/2.0811608jes.
[28] Barroux A, Delgado J, Orazem ME, Tribollet B, Laffont L, Blanc C. Electrochemical impedance spectroscopy study of the passive film for laser-beam-melted 17-4PH stainless steel. Corros Sci 2021;191:109750. https://doi.org/10.1016/j.corsci.2021.109750.
[29] Benoit M, Bataillon C, Gwinner B, Miserque F, Orazem ME, Sánchez-Sánchez CM, et al. Comparison of different methods for measuring the passive film thickness on metals. Electrochim Acta 2016;201:340–7. https://doi.org/10.1016/j.electacta.2015.12.173.
[30] Zhang Y, Hu Y, Li H, Gao Y, Wang Y, Feng H, et al. Martensitic transformation induced planar deformation of AlN nanoprecipitates in high nitrogen stainless steels. Int J Plast 2023;166:103631. https://doi.org/10.1016/j.ijplas.2023.103631.